

Limiting or Continuous Thermal Etching of First Row Transition Metal Oxides Using Acetylacetone and Ozone

Jonathan L. Partridge, Aziz I. Abdulagatov, David R. Zywootko, and Steven M. George*



Cite This: *Chem. Mater.* 2024, 36, 7151–7161



Read Online

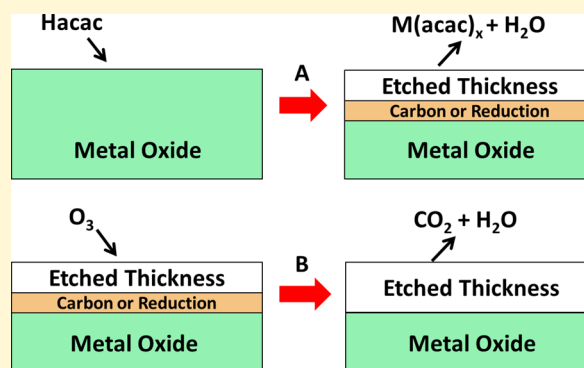
ACCESS |

Metrics & More

Article Recommendations

Supporting Information

ABSTRACT: The thermal etching of first row transition metal oxides was surveyed at 250 °C using acetylacetone (Hacac) and ozone (O₃). The metal oxides include Sc₂O₃, V₂O₅, VO₂, Cr₂O₃, Mn₂O₃, MnO, Fe₂O₃, Fe₃O₄, Co₃O₄, CoO, NiO, CuO, Cu₂O, and ZnO. The key measure of etching was the formation of volatile M(acac)_x etch products in the gas phase observed by in situ quadrupole mass spectrometry (QMS). Behavior consistent with continuous, unrestricted thermal etching during multiple Hacac minidoses was observed for ZnO, Mn₂O₃, and MnO. Various degrees of limiting, restricted behavior with respect to number of Hacac minidoses were observed for the other metal oxides. This self-limiting behavior could be used to define a thermal atomic layer etching (ALE) process. The limiting behavior was assessed using the time-resolved ion intensities for the M(acac)_x etch products during five sequential Hacac minidoses. O₃ was then used to refresh the metal oxide (1) by oxidizing the metal oxide or (2) by removing carbon species that could form during Hacac decomposition on some of the metal oxides. A final Hacac dose was then employed to check for an enhancement in ion intensity for the M(acac)_x etch products resulting from the O₃ exposure. Sc₂O₃, Cr₂O₃, MnO, Fe₃O₄, CoO, NiO, CuO, and ZnO all formed M(acac)_x etch products with the same oxidation state as the original metal oxide. In contrast, other metal oxides including V₂O₅, Mn₂O₃, and Co₃O₄ displayed M(acac)_x etch products with a lower oxidation state relative to the original metal oxide. This reduction may occur by oxygen loss from the metal oxide resulting from Hacac combustion. Two metal oxides, Fe₂O₃ and VO₂, displayed evidence for multiple M(acac)_x etch products that either stayed in the original oxidation state of the metal oxide or changed to a lower oxidation state. One metal oxide, Cu₂O, formed Cu(acac)₂ through a disproportionation reaction that produced metallic Cu on the surface. No etching was observed for MnO₂ and TiO₂. Mn₂O₃ and Co₃O₄ both showed strong evidence of Hacac combustion and formed CO₂ and H₂O during the Hacac exposures. Quartz crystal microbalance experiments at 200 °C confirmed the continuous, unrestricted thermal etching of ZnO atomic layer deposition (ALD) films during Hacac exposure. For Cu₂O, the observed etch product was Cu(acac)₂. Spectroscopic ellipsometry experiments on Cu₂O films at 180 °C showed evidence of disproportionation where Cu metal grows on the underlying Cu film during the thermal etching of Cu₂O. Hacac and O₃ can provide a halogen-free method for the thermal etching of most of the first row transition metals and their metal oxides.



1. INTRODUCTION

Atomic layer etching (ALE) uses two sequential, self-limiting surface reactions to create a highly controllable etch process.^{1,2} The first reaction is typically a surface modification, followed by a second reaction that leads to volatile release of the modified surface layer.^{1–3} ALE can be performed using either plasma or thermal methods. Plasma ALE uses energetic ions or neutrals to remove the modified surface layer and can be anisotropic.² Thermal ALE uses thermal reactions to remove the modified surface layer and can be isotropic.^{1,3}

Several thermal ALE pathways have been developed recently.³ One thermal ALE mechanism is fluorination and ligand exchange.^{3–5} The surface modification step involves fluorination of the surface of the substrate.⁶ Next, ligand exchange is used to form volatile products from the surface fluoride.^{7–9} This mechanism has been demonstrated for the

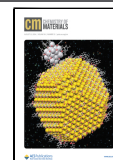
ALE of Al₂O₃,^{5,6,10–12} ZrO₂,^{11,12} and HfO₂.^{11–13} Another ALE mechanism is conversion followed by volatilization of the conversion layer.^{3,14} In this mechanism, a metal oxide is converted to a different metal oxide that has a volatile fluoride. The conversion layer is then spontaneously etched by a subsequent fluorination reaction. An example of this conversion mechanism is WO₃ ALE.¹⁴ Conversion reactions can also convert metal oxides to different metal oxides that can

Received: March 23, 2024

Revised: July 11, 2024

Accepted: July 12, 2024

Published: August 2, 2024



be etched using fluorination and ligand-exchange reactions. This conversion mechanism has been used for the ALE of Si,¹⁵ SiO₂,¹⁶ SiN_x,¹⁷ and Si_xGe_y.¹⁸

A new mechanism for thermal ALE is surface modification followed by ligand addition. During ligand addition, a precursor adds to the modified layer and becomes an L ligand on the metal center.¹⁹ This addition can volatilize the modified layer. The surface modification is usually chlorination and then ligand addition occurs on the metal chloride. The ligand addition mechanism has been demonstrated for Ni ALE using SO₂Cl₂ for chlorination and PMe₃ for ligand addition.²⁰ Co ALE has also been documented using SO₂Cl₂ for chlorination and tetramethylethylenediamine (TMEDA) for ligand addition.²¹ In addition, ALE for a variety of first row transition metal oxides such as Fe₂O₃, CoO, NiO, and ZnO have been demonstrated using SO₂Cl₂ for chlorination and TMEDA for ligand addition.²²

The β-diketonates can be used for ligand substitution and they are classified as LX ligands according to the covalent bond classification (CBC) method.¹⁹ These LX bidentate ligands raise the oxidation of the metal center by one.¹⁹ Perhaps the best known β-diketonates are acetylacetonate (Hacac) and hexafluoroacetylacetonate (Hhfac). Metal etching has been achieved through alternating oxidation and β-diketonate reactions.²³ Cu ALE has been demonstrated using oxidation with O₂ or ozone (O₃).²⁴ Subsequently, the copper oxide layer is removed using Hhfac to form Cu(hfac)₂ and H₂O.²⁴ Co ALE has also been demonstrated using Cl₂ for chlorination of the surface and Hhfac for volatilization of the cobalt chloride on the surface.²⁵

The β-diketonates can also be used for metal oxide ALE. The proposed ALE mechanism for metal oxides using Hacac and O₃ is shown in Figure 1. In the first reaction, Hacac reacts

to a higher oxidation state.²⁷ The O₃ reaction refreshes the metal oxide surface and enables further metal oxide thermal etching with Hacac.

Hacac has been documented for CoO ALE using Hacac and O₃.²⁷ Hacac removes Co as Co(acac)₂ during the Hacac exposure. Some Hacac decomposition then leads to the slow restriction of this etching reaction.²⁷ O₃ can then clean the surface and refresh the oxide surface. Hacac and O₃ have also been observed to change the oxidation state of the CoO surface.²⁷ O₃ oxidizes CoO to Co₃O₄. Hacac then reduces Co₃O₄ back to CoO through a combustion reaction.²⁷ Hacac has also been reported for ZnO ALE using Hacac and O₂ plasma.²⁶ Hacac is believed to remove Zn as Zn(acac)₂ before Hacac decomposes on the ZnO surface and stops the etching reaction. O₂ plasma is then thought to be required to clean the ZnO surface by removing the carbonaceous decomposition species.

The β-diketonates have also been employed for the thermal etching of a variety of metal oxides. Hhfac is effective for the dry etching of ZnO.²⁸ Hhfac can also etch iron oxide.²⁹ Hacac will react with γ-Al₂O₃ and lead to etching by producing Al(acac)₃.³⁰ Many studies have also reported the etching of copper oxide using Hhfac.^{31–33} Copper can also be etched at high rates by the oxidation of copper to copper oxide followed by Hhfac exposures.^{34,35} The oxidant and Hhfac can also be flowed simultaneously to etch copper.^{36,37}

This paper surveys the thermal etching of the first row transition metal oxides using Hacac and O₃ as the reactants at 250 °C. A custom quadrupole mass spectrometer was utilized to observe the volatile species during the thermal etching of metal oxide powders. Independent experiments for ZnO and Cu₂O flat substrates were performed using quartz crystal microbalance (QCM) and in situ spectroscopic ellipsometry (SE) measurements, respectively, to correlate the etching of flat samples with the volatile etch species observed from ZnO and Cu₂O powders. These combined investigations show the ability of Hacac to act as a halogen-free precursor to etch a large number of metal oxides. This thermal etching can have various degrees of self-limiting behavior to define an ALE process. Alternatively, this thermal etching can be continuous and proceed with no evidence of limiting behavior.

2. EXPERIMENTAL SECTION

2.1. Quadrupole Mass Spectrometry (QMS) Studies. The QMS reactor used in this study has been reported previously.²² This reactor uses two nested inlet lines that meet just before the heated powder bed to minimize cross-contamination of the reactor foreline. The QMS reactor was designed to allow the etch products to expand into vacuum and define a molecular beam.⁸ The molecular beam then passes through a skimmer and travels with line-of-sight into the differentially pumped region of the QMS ionizer.⁸ This arrangement maximizes the sensitivity to detect the etch products. All experiments were conducted at a powder bed temperature of 250 °C.

The dose sequence used in this study was designed to test for the self-limitation of volatile etch species during Hacac exposure. In addition, the dose sequence also determined the effect of an O₃ dose on the subsequent Hacac dose. The dose sequence consisted of five sequential Hacac minidoses with dose times of 300 s, one O₃ dose of 300 s, and one final Hacac dose of 300 s. The purge time between all doses to allow N₂ gas to purge the powder bed was 300 s. The average precursor partial pressure was ≈2.3 Torr for Hacac and O₃. The pressure of the flowing N₂ gas was ≈2.6 Torr. Hacac was purchased from Millipore Sigma (Reagentplus, 99%) and loaded under inert atmosphere. O₃ was generated using prepurified O₂ and an ozone

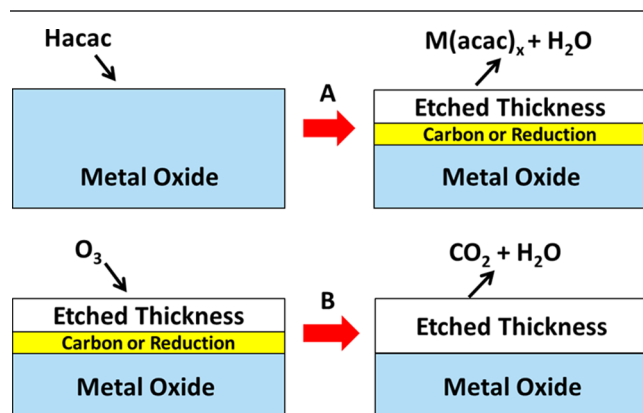


Figure 1. Proposed mechanism for metal oxide ALE. (a) Hacac reacts with metal oxide by acac substitution for oxygen to form M(acac)_x and H transfer to oxygen to form H₂O. (b) O₃ provides oxidative cleaning.

with the metal oxide surface to form volatile metal acetylacetonates where acac substitutes for oxygen in the original metal oxide. H₂O is also formed by hydrogen transfer from Hacac to oxygen in the metal oxide. Hacac may also decompose on the metal oxide surface during the reaction and leave carbon residue. This carbon residue may restrict the metal oxide surface from additional etching.²⁶ Hacac may also reduce the oxidation state of the metal oxide.²⁷ In the second reaction, O₃ can react with carbon residue to form CO₂ and H₂O combustion products. O₃ can also oxidize the metal oxide

generator (LG-14, Ozone Engineering) with an average O₃ concentration of 5 wt%.

The powders used in these QMS experiments were Sc₂O₃ (5 μm, 99.999% super purity, US-Nano), TiO₂ (165 nm, 99.9%, Rutile, US-Nano), V₂O₅ (99.95% trace metals basis, Sigma), VO₂ (99% trace metals basis, Sigma), Cr₂O₃ (60 nm, 99+%, Hexagonal, US-Nano), MnO₂ (99%, ReagentPlus, Sigma), Mn₂O₃ (30 nm, 99.2%, US-Nano), MnO (99%, 60 mesh, Sigma), Fe₂O₃ (30 nm, 99.5+% high purity, Alpha, US-Nano), Fe₃O₄ (8 nm, 99.9%, Spinel, US-Nano), Co₃O₄ (30–50 nm, 99.5+%, US-Nano), CoO (50 nm, 99.7%, US-Nano), NiO (15–35 nm, 99.5+% High Purity, US-Nano), CuO (25–55 nm, 99.95+%, US-Nano), Cu₂O (18 nm, 99.86%, US-Nano), and ZnO (80–200 nm, 99.9+%, US-Nano).

Initial powder masses loaded into the chamber varied based on particle size and density, ranging from 15 mg to 123 mg. Powders were weighed before and after exposure to the pulse sequence. A percent mass loss of the powders after etching was used to verify material removal. Percent mass losses ranged from less than 1% to as high as 76%. Small mass losses can be attributed to minor mass losses during sample transfer.

Knowing the particle diameter and assuming spherical particles, the percentage mass loss can be converted to a fraction mass loss. The fraction mass retained (1-fraction mass loss) can then be utilized to estimate the etch thickness resulting from the pulse sequence. Mass is directly proportional to particle volume. The volume of a spherical particle is $V = 4/3\pi r^3$ where r is the particle radius. The etch thickness can then be derived from the fraction mass retained and the initial radius of the particle, r_1 , according to

$$\text{Etch thickness} = r_1(1 - (\text{fraction mass retained})^{1/3}) \quad (1)$$

The initial particle radius was obtained from the particle suppliers as reported above.

QMS results were obtained using a quadrupole mass spectrometer (Extrel, MAX-QMS Flanged Mounted System).^{8,22} An electron ionization energy of 70 eV was employed in the experiments. The ionizer and analyzer were positioned perpendicular to the incoming molecular beam. QMS scans were conducted with an m/z range from 2 to 500 with 1 s per scan. The isotopic distributions of the volatile etch species were calculated from the naturally occurring isotopic abundances of each compound. For example, for Zn(acac)₂ (acac = C₅H₇O₂), all 5 isotopes of Zn (⁶⁴Zn, ⁶⁶Zn, ⁶⁷Zn, ⁶⁸Zn, and ⁷⁰Zn), and both isotopes of C (¹²C, ¹³C) were used to generate isotopic patterns. The expected relative abundance was calculated for each m/z value.

2.2. Quartz Crystal Microbalance (QCM) Studies. The quartz crystal microbalance (QCM) experiments were performed in a viscous flow reactor.³⁸ The quartz crystal used for the QCM studies (polished, Au-coated, RC cut, 6 MHz, Phillip Technologies) was placed in a sensor head (Inficon) and sealed with a high temperature silver epoxy (Epo-Tek H21D, Epoxy Technology Inc.). The QCM head was placed in the isothermal region of the reactor. A constant N₂ gas flow on the back of the QCM was used to prevent interaction of precursors with the backside of the QCM crystal.³⁸ The changes in resonant frequency of the quartz crystal were recorded and converted to mass using a thin film deposition monitor (Maxtek TM-400, Inficon).

ZnO films were deposited on an Au-coated QCM crystal using ZnO atomic layer deposition (ALD) with diethylzinc (DEZ; 52 wt % Zn, Sigma-Aldrich) and H₂O as the reactants at 150 °C.³⁹ The ZnO ALD films had a thickness of ~33 nm after 1600 ALD cycles with an average growth rate of ~2 Å/cycle. The reactor was then heated to 200 °C and allowed to thermally equilibrate before thermal etching using Hacac. Thermal etching was performed using Hacac at a pressure of 500 mTorr over a N₂ background pressure of 1.0 Torr.

2.3. Spectroscopic Ellipsometry (SE) Studies. The reactor used for the spectroscopic ellipsometry (SE) studies was equipped with an in situ spectroscopic ellipsometer (J.A. Woollam model M-2000UI).¹⁵ The walls of the reactor were kept at 160 °C. The sample holder was differentially heated to achieve the desired sample temperature of 180 °C. For the SE experiments, an initial Cu film

with a thickness of ~35 nm was deposited using physical vapor deposition (PVD) on a Si wafer with a tantalum diffusion barrier film.

The copper surface was oxidized in the same reactor by several doses of ozone at 180 °C. O₃ was produced with prepurified oxygen as the feed gas in an O₃ generator (O3ONIA CFS-1A). The O₃ output was ~15 wt %. The copper oxide film was etched by exposing Hacac (Millipore Sigma) statically at a partial pressure of 0.7 Torr with a dose time of 1 s and a hold time of 5 s. The Hacac pressure refers to the partial Hacac pressure with respect to a N₂ background pressure of ~1 Torr. UHP grade N₂ (99.9999%, Airgas) was used as the carrier and purge gas. The changes in the Cu₂O and Cu film thicknesses were simultaneously determined by SE measurements during Hacac exposures.

3. RESULTS AND DISCUSSION

3.1. Thermal Etching of Cr₂O₃ with Hacac and O₃. QMS studies were performed to study thermal etching during sequential exposures of Hacac and O₃ on Cr₂O₃ powders at 250 °C. Chromium is a Group 6 transition metal. The QMS ion signals for Cr(acac)₂⁺ and Cr(acac)₃⁺ are displayed in Figure 2a,b, respectively, during an Hacac exposure at 2.3 Torr

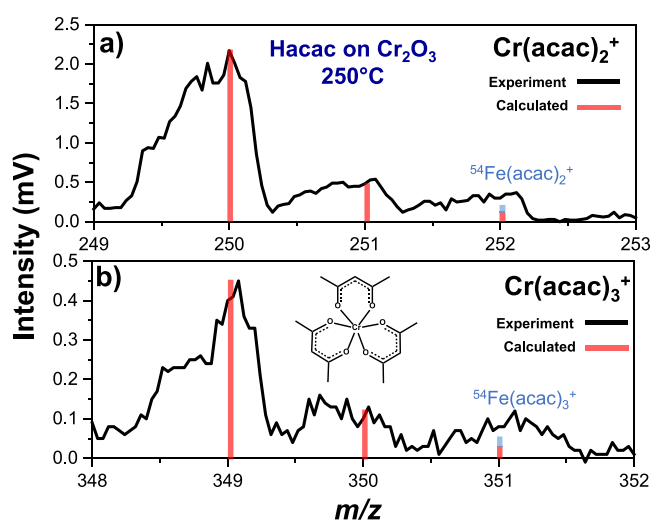


Figure 2. Mass spectra of (a) Cr(acac)₂⁺ ion intensity and (b) Cr(acac)₃⁺ ion intensity observed during Hacac exposure on Cr₂O₃ powder at 250 °C.

on Cr₂O₃ powder at 250 °C. Cr(acac)₃ is the expected source of these QMS ion signals. Cr(acac)₃ has a reported melting point of 216 °C and has volatility at 250 °C.^{40,41}

Metal acetylacetonates with a formula M(acac)_x will generally have their largest ion signals during mass spectrometry at M(acac)_{x-1}⁺. Figure 2a shows Cr(acac)₂⁺ with an intensity of 2.2 mV at m/z 250. This fragment has a larger intensity than the Cr(acac)₃⁺ parent ion. The Cr(acac)₃⁺ ion signal in Figure 2b has an intensity of 0.5 mV at m/z 349. This ratio is consistent with the reported electron impact ionization pattern for Cr(acac)₃. The signal intensity for m/z 349 is 29.7% of the signal intensity for m/z 250.⁴²

In both Figure 2a,b, some signal intensity can be attributed to cracks of ⁵⁴Fe(acac)₃. In addition, trace cracks of both Cr(acac)₃ and Fe(acac)₃ can be observed during the experiments for all the metal oxide powders in addition to Cr₂O₃, Fe₂O₃ and Fe₃O₄. For the powders not containing Cr or Fe, the Cr(acac)₃ and Fe(acac)₃ signals are attributed to the etching of the oxidized Cr and Fe components of the stainless steel reactor surfaces. For these powders, the signal intensity

ratio of $\text{Cr}(\text{acac})_2^+$ at m/z 250 to $\text{Fe}(\text{acac})_2^+$ at m/z 254 was 26.3%. Based on this ratio and the observed $\text{Fe}(\text{acac})_2^+$ signal during the experiments on the Cr_2O_3 powder, 42% of the observed $\text{Cr}(\text{acac})_x^+$ signal can be attributed to contributions from the 304 stainless steel reactor surfaces. Compared with an empty chamber control experiment, the signal intensity of $\text{Cr}(\text{acac})_3^+$ in Figure 2b is more than doubled when Cr_2O_3 powder is in the sample holder. These results indicate that the high surface area Cr_2O_3 powder contributes substantially to the ion signal for $\text{Cr}(\text{acac})_3$ in Figure 2b.

Figure 3 shows the ion intensities for Hacac^+ , O_2^+ , $\text{Cr}(\text{acac})_2^+$, and H_2O^+ during Hacac and O_3 exposures on

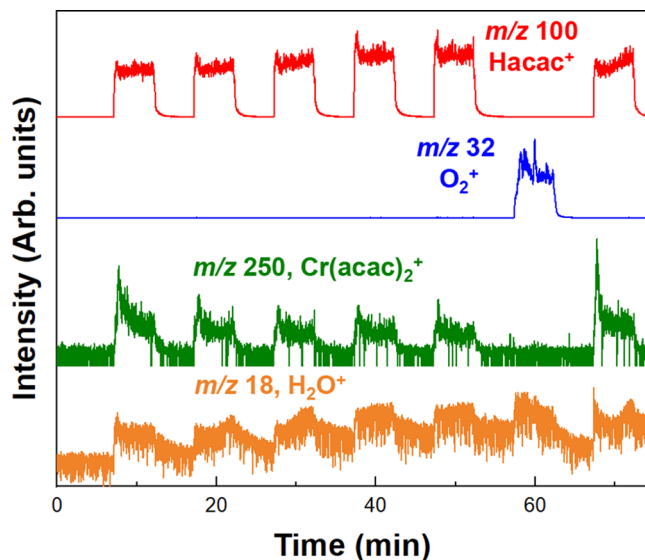


Figure 3. Ion signal intensities for Hacac^+ , O_2^+ , $\text{Cr}(\text{acac})_2^+$, and H_2O^+ during Hacac and O_3 exposures on Cr_2O_3 powder at 250 °C.

Cr_2O_3 at 250 °C. The Hacac^+ and O_2^+ signals monitor the dosing sequence of Hacac and O_3 . This dosing sequence consisted of five 300 s Hacac minidoses, one 300 s O_3 dose, and one 300 s Hacac dose. Each dose was separated by a 300 s purge when N_2 flowed over the powder bed. An ion signal for O_3^+ was not observed at m/z 48. This dosing sequence allowed for the observation of: (1) the $\text{M}(\text{acac})_x^+$ etch product; (2) a H_2O^+ signal concurrent with the $\text{M}(\text{acac})_x^+$ etch products; (3) changes in $\text{M}(\text{acac})_x^+$ ion signal intensity with a series of sequential Hacac minidoses, and (4) a comparison of $\text{M}(\text{acac})_x^+$ ion signal intensities before and after O_3 exposures.

Figure 3 shows the observation of the $\text{Cr}(\text{acac})_3$ etch product as indicated by its largest $\text{Cr}(\text{acac})_2^+$ fragment at m/z 250. The $\text{Cr}(\text{acac})_2^+$ ion signal intensity decreases slowly with each successive Hacac dose. The normalized integrated intensities for $\text{Cr}(\text{acac})_2^+$ ion signals from the five Hacac minidoses relative to the first Hacac minidose are 100, 50, 48, 47, and 45%. These results indicate that Hacac is not ideal for Cr_2O_3 ALE because the $\text{Cr}(\text{acac})_2^+$ signal intensity is not strongly limiting versus Hacac minidoses. This slow decrease could indicate a buildup of carbon species on the powder surface that limits the etching reaction. H_2O is the expected volatile product of the hydrogen transfer reaction during Hacac exposures. The H_2O^+ ion signal coincides with the $\text{Cr}(\text{acac})_2^+$ ion signal during all the Hacac doses.

During the O_3 exposure, the H_2O^+ ion signal in Figure 3 rises above the background signal level. This H_2O signal is

expected from the combustion by O_3 of surface hydrocarbon species that may be restricting the Cr_2O_3 etching. After the O_3 exposure, the signal intensity of $\text{Cr}(\text{acac})_2^+$ in Figure 3 shows an enhancement. This behavior is consistent with the cleaning of the Cr_2O_3 powder surface.

The Cr_2O_3 powder samples were weighed before and after the etching experiments. The Cr_2O_3 powder showed a 16.7% mass loss after etching using the reactant pulse sequence. Given spherical Cr_2O_3 particles with an initial radius of 30 nm, this 16.7% mass loss (or 0.833 fraction mass retained) yields an estimated etch thickness of 18 Å from the initial particles after the pulse sequence in Figure 3. This etch thickness is reasonable because the Cr_2O_3 etching by Hacac is weakly limiting and the pulse sequence includes a second Hacac dose after O_3 cleaning.

3.2. Thermal Etching of ZnO with Hacac and O_3 . QMS studies were also conducted to examine the thermal etching of ZnO during exposures of Hacac and O_3 at 250 °C. Zinc is a transition metal on the periodic table in Group 12. Figure 4

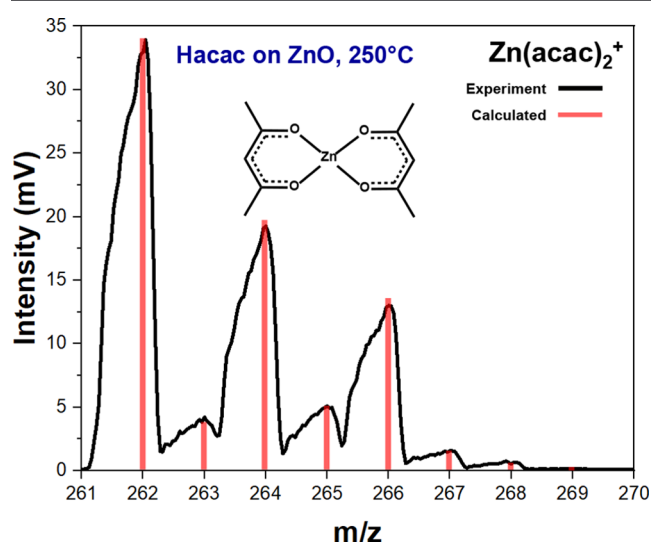


Figure 4. Mass spectrum of $\text{Zn}(\text{acac})_2^+$ ion intensity during Hacac exposure on ZnO powder at 250 °C.

shows the mass spectrum of $\text{Zn}(\text{acac})_2^+$ during Hacac exposure on ZnO powder at 250 °C. This mass spectrum is consistent with the five isotopes of Zn (^{64}Zn , ^{66}Zn , ^{67}Zn , ^{68}Zn , and ^{70}Zn) and both isotopes of C (^{12}C , ^{13}C) in $\text{Zn}(\text{acac})_2$. The largest signal at m/z 262 is consistent with $^{64}\text{Zn}(\text{acac})_2$. Only the +2 oxidation state has been previously reported for zinc acetylacetonate and ZnO.

Figure 5 shows the time-resolved ion intensities for Hacac^+ , O_2^+ , $\text{Zn}(\text{acac})_2^+$, and H_2O^+ during Hacac and O_3 exposures on ZnO at 250 °C. Unlike the slowly limiting behavior observed for Hacac exposures on Cr_2O_3 in Figure 3, the $\text{Zn}(\text{acac})_2^+$ ion intensity does not decrease during five sequential Hacac minidoses on ZnO powder in Figure 5. After the first Hacac minidose, a decrease in $\text{Zn}(\text{acac})_2^+$ ion intensity is not observed for the following four Hacac minidoses. The H_2O^+ ion intensity also follows the $\text{Zn}(\text{acac})_2^+$ signal and is constant during the Hacac minidoses.

These observations indicate that Hacac can continuously etch ZnO. This behavior suggests that the possible Hacac decomposition on the ZnO surface is minimal and does not restrict the ZnO etching. The lack of self-limiting behavior

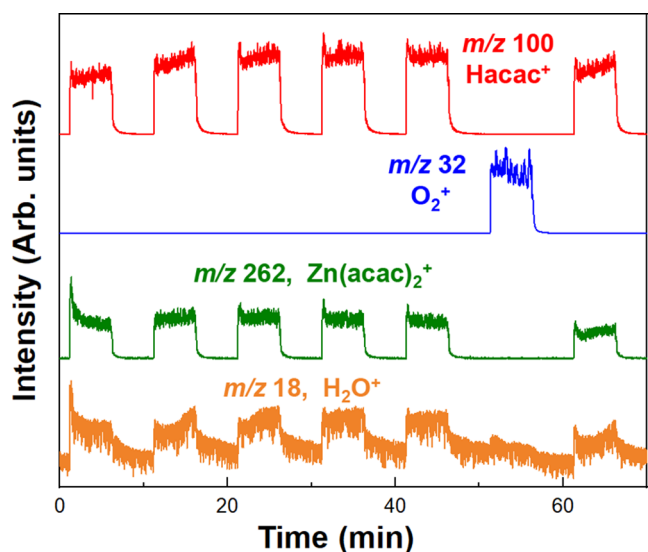


Figure 5. Ion signal intensities for Hacac^+ , O_2^+ , $\text{Zn}(\text{acac})_2^+$, and H_2O^+ during Hacac and O_3 exposures on ZnO powder at 250 °C.

indicates that Hacac is not a candidate for ZnO ALE. The low H_2O^+ ion intensity during the O_3 exposure in Figure 5 also argues that the O_3 does not produce combustion products. There is little H_2O produced because Hacac has presumably not decomposed on the ZnO surface.

The ZnO powder samples were weighed before and after the etching experiments. The ZnO powder had a mass loss of 42.3% after exposure to the pulse sequence in Figure 5. Given spherical ZnO particles with an initial radius of 70 nm, this 42.3% mass loss (or 0.577 fraction mass retained) yields an estimated etch thickness of 117 Å from the initial particles after the pulse sequence in Figure 5. This large etch material thickness is consistent with the greater amount of material removal expected from continuous etching.

Experiments on ZnO ALD films on flat substrates were performed to corroborate the thermal etching of ZnO by Hacac observed by the QMS experiments on ZnO powder. Figure 6 shows the mass loss versus time during the etching of an ZnO ALD film on a QCM sensor by Hacac at 200 °C.

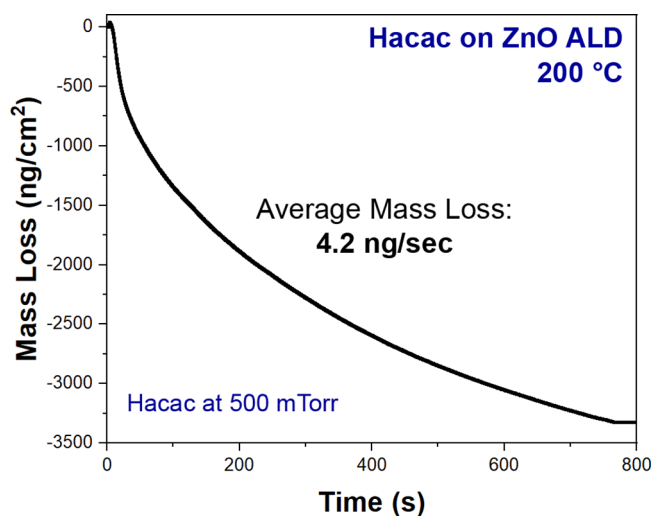


Figure 6. Mass loss during spontaneous etching of ZnO ALD film during Hacac exposure at 500 mTorr at 200 °C.

During this experiment, Hacac was introduced into the reactor and maintained an average pressure of 0.5 Torr over the 1.0 Torr pressure from the N_2 flow. The Hacac exposure in Figure 6 led to the complete removal of the ZnO ALD film. The average mass loss versus time during the Hacac exposure was 4.2 ng/s.

These results are not consistent with the previous reported literature on ZnO ALE using sequential Hacac and O_2 plasma exposures.²⁶ This previous study was performed using ZnO ALD films deposited at 250 °C.²⁶ There may have been DEZ decomposition and carbon contamination of the ZnO ALD films during deposition at 250 °C.²⁶ The ALD window for ZnO ALD is typically reported between 100 and 200 °C.⁴³ At higher temperatures of 250 °C, there could have been carbon species produced by DEZ decomposition that required oxidative cleaning. Alternatively, the O_2 plasma used in the pulse sequence of the previous study may have modified the ZnO surface and led to Hacac decomposition on this modified surface.²⁶

3.3. Thermal Etching of V_2O_5 and VO_2 with Hacac and O_3 . The thermal etching of V_2O_5 and VO_2 was also explored using Hacac and O_3 exposures. Vanadium is a Group 5 transition metal. Figure 7 shows the mass spectrum of

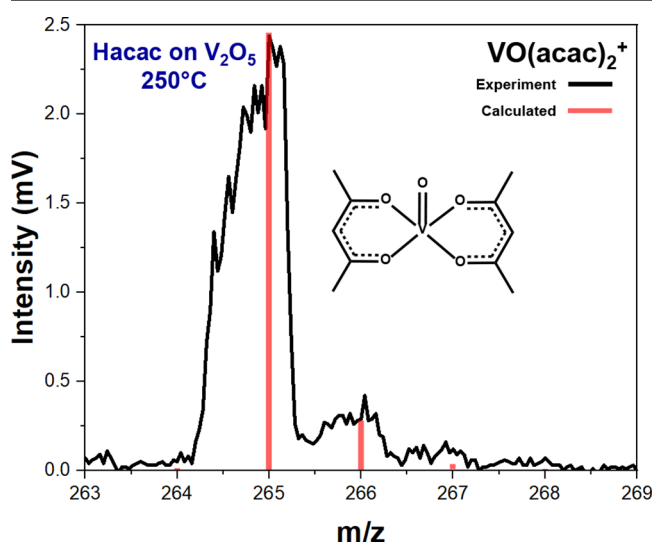


Figure 7. Mass spectrum of $\text{VO}(\text{acac})_2^+$ ion intensity during Hacac exposure on V_2O_5 powder at 250 °C.

$\text{VO}(\text{acac})_2^+$ observed during Hacac exposure on V_2O_5 powder at 250 °C. Earlier studies have also identified $\text{VO}(\text{acac})_2$ as the reaction product.³³ The observation of $\text{VO}(\text{acac})_2^+$ from $\text{VO}(\text{acac})_2$ indicates that the vanadium center has lowered its oxidation state in going from +5 in V_2O_5 to +4 in $\text{VO}(\text{acac})_2$. $\text{VO}(\text{acac})_2$ has a melting point of 235 °C and high volatility at 250 °C.⁴⁴

Figure 8 shows the two distinct etch products observed during Hacac exposure on VO_2 powder at 250 °C. Figure 8a shows the mass spectrum of $\text{VO}(\text{acac})_2^+$ during Hacac exposure on VO_2 powder at 250 °C. The $\text{VO}(\text{acac})_2^+$ ion signal is the same as observed for Hacac exposure on V_2O_5 powder in Figure 7. In addition, Figure 8b shows the mass spectrum of $\text{V}(\text{acac})_3^+$ during Hacac exposure on VO_2 powder at 250 °C. Figure 8a,b were both taken from different mass ranges of the same full mass spectrum. $\text{V}(\text{acac})_3$ did not appear during Hacac exposures on V_2O_5 powder. $\text{V}(\text{acac})_3^+$ ion signal

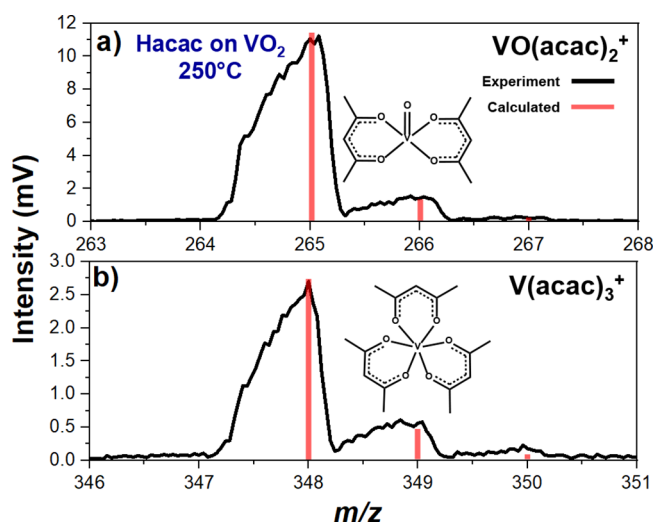


Figure 8. Mass spectra of (a) $\text{VO}(\text{acac})_2^+$ ion intensity and (b) $\text{V}(\text{acac})_3^+$ ion intensity during Hacac exposure on VO_2 powder at 250 °C.

is observed only when the oxidation state of the starting metal oxide is +4 in VO_2 .

VO_2 has two pathways for thermal etching during Hacac exposures. VO_2 can remain in the +4 oxidation state of VO_2 to form $\text{VO}(\text{acac})_2$. Alternatively, VO_2 can reduce to form the $\text{V}(\text{acac})_3$ etch product in the +3 oxidation state. $\text{V}(\text{acac})_3$ has a reported melting point of 181–184 °C and has volatility at 250 °C.⁴¹

Figure 9 shows the ion intensities for Hacac⁺, O_2^+ , $\text{VO}(\text{acac})_2^+$, and $\text{V}(\text{acac})_3^+$ during Hacac and O_3 exposures

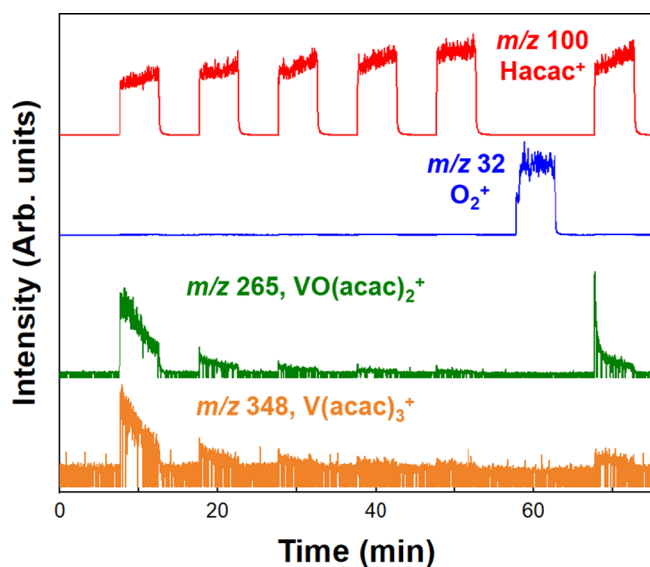


Figure 9. Ion signal intensities for Hacac⁺, O_2^+ , $\text{VO}(\text{acac})_2^+$, and $\text{V}(\text{acac})_3^+$ during Hacac and O_3 exposures on VO_2 at 250 °C.

on VO_2 powder at 250 °C. Both $\text{V}(\text{acac})_3$ and $\text{VO}(\text{acac})_2$ etch products decrease during the first five Hacac minidoses. The normalized integrated intensities from the five Hacac minidoses for $\text{VO}(\text{acac})_2^+$ relative to the first Hacac minidose are 100, 21, 8, 4, and 4%. The ion signals fall almost to noise level for both etch products after five Hacac minidoses. After exposure to O_3 , the next Hacac dose shows a large

enhancement for the $\text{VO}(\text{acac})_2^+$ ion signal. The reappearance of the $\text{VO}(\text{acac})_2^+$ ion signal indicates that O_3 cleaned the VO_2 surface. The self-limiting behavior versus Hacac exposures and the ability of O_3 to clean the VO_2 surface indicates that VO_2 ALE could be accomplished using sequential Hacac and O_3 exposures.

After the O_3 cleaning, Figure 9 shows that the signal enhancement for $\text{VO}(\text{acac})_2^+$ was much larger than for $\text{V}(\text{acac})_3^+$. The O_3 cleaning may have partially oxidized VO_2 to V_2O_5 . The etch product from V_2O_5 was exclusively $\text{VO}(\text{acac})_2^+$. The VO_2 powder had a mass loss of 37.9% after the pulse sequence shown in Figure 9. This mass loss is more than double the 16.5% mass loss observed for the similar pulse sequence applied to the V_2O_5 powder (results not shown). The signal intensities during the pulse sequence on V_2O_5 powder also showed decreasing $\text{VO}(\text{acac})_2^+$ signals versus Hacac doses. In addition, there was an increase in $\text{VO}(\text{acac})_2^+$ signal intensity after the O_3 exposure. Estimates of etch thicknesses from the mass losses were not possible because the particle diameters were not available.

3.4. Thermal Etching of Mn_2O_3 and MnO with Hacac and O_3 . The thermal etching of Mn_2O_3 was observed using Hacac exposures at 250 °C. Manganese is on the periodic table in Group 7. Figure 10 shows the mass spectrum for

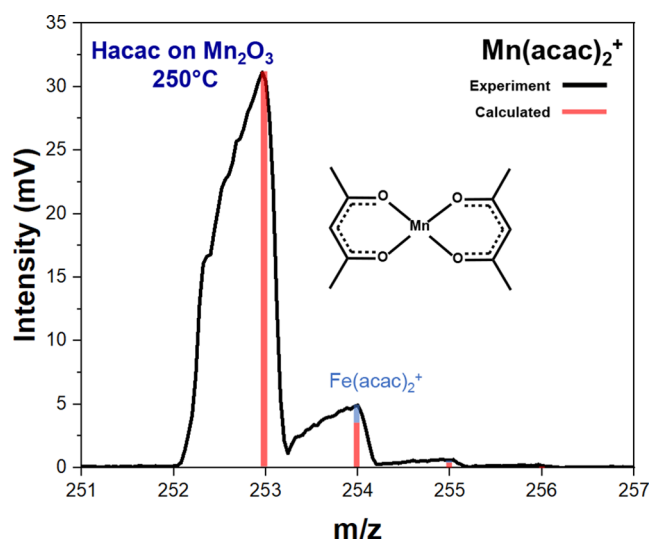


Figure 10. Mass spectrum of $\text{Mn}(\text{acac})_2^+$ during Hacac exposure on Mn_2O_3 powder at 250 °C.

$\text{Mn}(\text{acac})_2^+$ during Hacac exposure on Mn_2O_3 powder at 250 °C. Mn has a single isotope with a mass of 55 amu. The isotopic signature results from ^{13}C in the acac ligands. A small contribution from $\text{Fe}(\text{acac})_2^+$ is also observed at m/z 254.

$\text{Mn}(\text{acac})_3$ has a melting point of 159–161 °C and $\text{Mn}(\text{acac})_2$ has a melting point of 248–250 °C.⁴⁵ Based on the lower reported melting point, $\text{Mn}(\text{acac})_3$ might be expected to have greater volatility at 250 °C than $\text{Mn}(\text{acac})_2$. However, $\text{Mn}(\text{acac})_3$ at m/z 352 was not observed in the mass spectrum. The reported mass spectrum for $\text{Mn}(\text{acac})_3$ shows a peak for $\text{Mn}(\text{acac})_3^+$ at m/z 352 that is 13.5% of the intensity of $\text{Mn}(\text{acac})_2^+$ at m/z 253.⁴⁶ The absence of ion intensity at m/z 352 in this study suggests that the volatile Mn-containing etch product is $\text{Mn}(\text{acac})_2$ and not $\text{Mn}(\text{acac})_3$. The higher melting temperature for $\text{Mn}(\text{acac})_2$ may be related to its trimeric structure in the solid state.⁴⁷

The mechanism by which Mn_2O_3 reduces to form $\text{Mn}(\text{acac})_2$ in the +2 oxidation state instead of $\text{Mn}(\text{acac})_3$ in the +3 oxidation state can be explained by the time-resolved ion intensities. Figure 11 shows the ion intensities for Hacac^+ ,

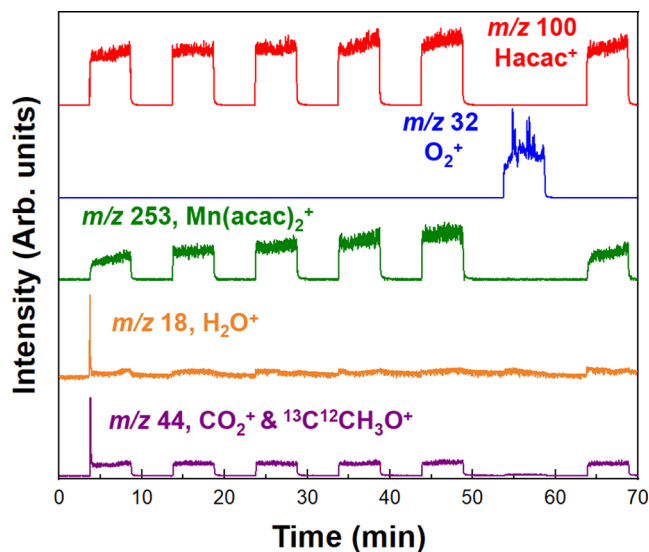


Figure 11. Ion signal intensities for Hacac^+ , O_2^+ , H_2O^+ , m/z 44, and $\text{Mn}(\text{acac})_2^+$ during Hacac and O_3 exposures on Mn_2O_3 powder at 250 °C.

O_2^+ , H_2O^+ , m/z 44 and $\text{Mn}(\text{acac})_2^+$ during Hacac and O_3 exposures on Mn_2O_3 powder at 250 °C. The first five seconds of the first Hacac minidose on Mn_2O_3 in Figure 11 displays a large spike in the intensities for H_2O and CO_2 combustion products. The spike in the H_2O^+ and CO_2^+ ion signals is consistent with the combustion of Hacac on the Mn_2O_3 surface. This combustion would remove oxygen from Mn_2O_3 and reduce Mn_2O_3 to MnO. A similar reduction in oxidation state was observed after Hacac exposures on Co_3O_4 . During CoO ALE, the oxidation state switched between +2 in CoO after Hacac exposures to +3/+2 in Co_3O_4 after O_3 exposures.²⁷ There is also a chance that CO_2 is produced by Hacac reacting with a reactive oxygen reservoir in Mn_2O_3 after O_3 exposures.⁴⁸

The $\text{Mn}(\text{acac})_2^+$ ion signal at m/z 253 in Figure 11 grows progressively during the five sequential Hacac minidoses. This behavior is consistent with the unrestricted etching of Mn_2O_3 by Hacac. The lack of limiting behavior versus Hacac exposure indicates that Hacac is not a possible candidate for Mn_2O_3 ALE. Separate experiments on MnO powders (results not shown) were similar to the results in Figure 11. However, the results on MnO powders did not have the initial spike of CO_2 and H_2O combustion products. After the Mn_2O_3 powder is reduced to MnO by the first Hacac dose, the results for the initial Mn_2O_3 and MnO powders were nearly identical. The progressive increase of the $\text{Mn}(\text{acac})_2^+$ ion signals in Figure 11 may be caused by the continued reduction of Mn_2O_3 to MnO with consecutive Hacac exposures.

The signal intensity for m/z 44 in Figure 11 is attributed to a combination of CO_2^+ and $^{13}\text{C}^{12}\text{CH}_3\text{O}^+$. $^{13}\text{C}^{12}\text{CH}_3\text{O}^+$ is 2.5% of the intensity of $^{12}\text{C}_2\text{H}_3\text{O}^+$ at m/z 43. $^{12}\text{C}_2\text{H}_3\text{O}^+$ is the largest ion signal resulting from electron impact ionization of Hacac. During the spike at the beginning of the first Hacac minidose, m/z 44 reaches a maximum of 38% the intensity of m/z 43. This behavior is consistent with CO_2 evolution during the first Hacac minidose.

The Mn_2O_3 powder had a mass loss of 61.1% after exposure to the pulse sequence. Given spherical Mn_2O_3 particles with an initial radius of 15 nm, this 61.1% mass loss (or 0.389 fraction mass retained) yields an estimated etch thickness of 41 Å from the initial particles after the pulse sequence in Figure 11. This large etch thickness is consistent with the greater amount of material removal expected from continuous etching. In comparison, the MnO powder had a mass loss of 10.0% after exposure to the same pulse sequence. Particle diameters were not available to estimate the etch thickness.

MnO_2 was also examined and did not reveal any Mn-containing etch products. The MnO_2 powder also displayed a mass loss of only 0.9% after the pulse sequence. This mass loss is negligible and can be attributed to sample transfer losses. These results indicate that MnO_2 is a more stable oxide than Mn_2O_3 with respect to Hacac combustion on the oxide surface.

3.5. Thermal Etching of Cu_2O and CuO with Hacac and O_3 . Thermal etching of Cu_2O and CuO was observed using Hacac exposures at 250 °C. Copper is a Group 11 transition metal. Figure 12 shows the mass spectrum of

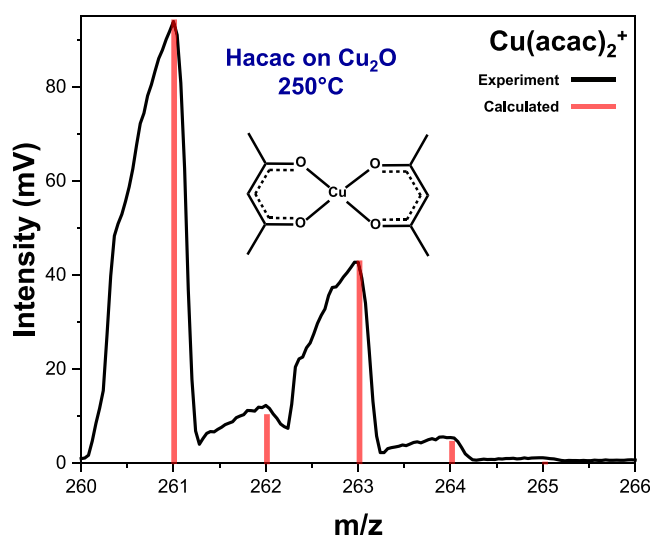


Figure 12. Mass spectrum of $\text{Cu}(\text{acac})_2^+$ ion intensity during Hacac exposure on Cu_2O powder at 250 °C.

$\text{Cu}(\text{acac})_2^+$ during Hacac exposure on Cu_2O powder at 250 °C. Both Cu_2O and CuO formed $\text{Cu}(\text{acac})_2$ during Hacac exposures. The calculated mass spectrum for $\text{Cu}(\text{acac})_2^+$ shown in Figure 12 is based on the ^{63}Cu and ^{65}Cu isotopes and the ^{12}C and ^{13}C isotopes in the acac ligands. There is excellent agreement between the experimental and calculated results for $\text{Cu}(\text{acac})_2^+$. No other Cu-containing species were observed in the mass spectrum between $\text{Cu}(\text{acac})_2^+$ located around m/z 261 and higher m/z values up to m/z 500.

The time-resolved ion signal intensities during Hacac doses on Cu_2O show restrictive behavior. Figure 13 displays the ion intensities for Hacac^+ , O_2^+ , H_2O^+ , m/z 44, and $\text{Cu}(\text{acac})_2^+$ during Hacac and O_3 exposures on Cu_2O powder at 250 °C. The signal intensity of $\text{Cu}(\text{acac})_2^+$ decreases with each sequential Hacac minidose. The normalized integrated intensities from the five Hacac minidoses for $\text{Cu}(\text{acac})_2^+$ relative to the first Hacac minidose are 100, 55, 47, 36, and 35%. There is also a signal intensity enhancement for the $\text{Cu}(\text{acac})_2^+$ ion intensity during the Hacac dose following the O_3 exposure. In addition, the signal intensity for H_2O^+ rises

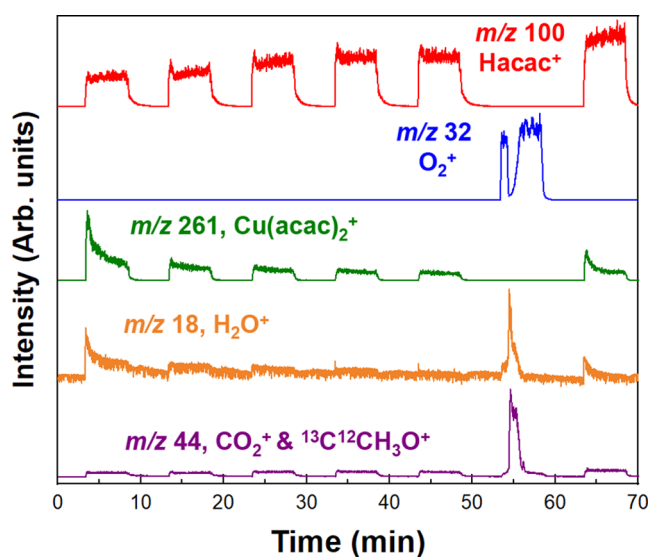


Figure 13. Ion signal intensities for Hacac⁺, O₂⁺, H₂O⁺, *m/z* 44, and Cu(acac)₂⁺ during Hacac and O₃ exposures on Cu₂O powder at 250 °C.

above the noise level with each Hacac dose and tracks the Cu(acac)₂⁺ ion signal intensity. The limiting behavior versus Hacac exposures and the ability of O₃ to clean the Cu₂O surface indicates that Cu₂O ALE may be possible using sequential Hacac and O₃ exposures.

During the O₃ exposure in Figure 13, there is a dramatic spike in CO₂ and H₂O combustion products. Both CO₂⁺ and H₂O⁺ ion signals rise simultaneously as the O₂⁺ ion signal shows a corresponding drop in intensity. Typically, the H₂O and CO₂ signals are observed above noise levels during each O₃ dose for many other metal oxides. However, this large spike is only observed for Cu₂O in Figure 13 and CuO (results not shown). This behavior indicates a more substantial decomposition of Hacac on the copper oxides compared with the other metal oxides. Signal at *m/z* 44 for all the Hacac doses in Figure 13 is around the expected 2.5% of the ¹³C¹²CH₃O ion intensity resulting from electron impact ionization of the Hacac precursor. There is no indication of CO₂ evolution during the Hacac exposures.

The Cu₂O powder had a mass loss of 45.1% after exposure to this pulse sequence. Given spherical Cu₂O particles with an initial radius of 9 nm, this 45.1% mass loss (or 0.549 fraction mass retained) yields an estimated etch thickness of 16 Å from the initial particles after the pulse sequence in Figure 13. In comparison, the CuO powder had a mass loss of 35.7% after exposure to this pulse sequence. Given spherical CuO particles with an initial radius of 20 nm, this 35.7% mass loss (or 0.643 fraction mass retained) yields an estimated etch thickness of 27 Å from the initial particles after the pulse sequence.

The etch products and time-resolved ion intensities are similar for the Cu₂O and CuO powders. However, there is an effect that is unique for the Cu₂O powder. Cu₂O is the only metal oxide in this study that is found in the +1 oxidation state. For a stoichiometric reaction that forms Cu(acac)₂ in the +2 oxidation state, the other Cu atom in Cu₂O must decrease to the +0 oxidation state of Cu metal.³³ The formation of +2 and 0 oxidation states from +1 oxidation states is a disproportionation reaction. Additional studies were conducted to attempt to observe this disproportionation reaction during the Hacac exposure.

Spectroscopic ellipsometry studies were performed on a flat copper sample with a Cu₂O film on the top during Hacac exposure. Figure 14 shows the spectroscopic ellipsometry

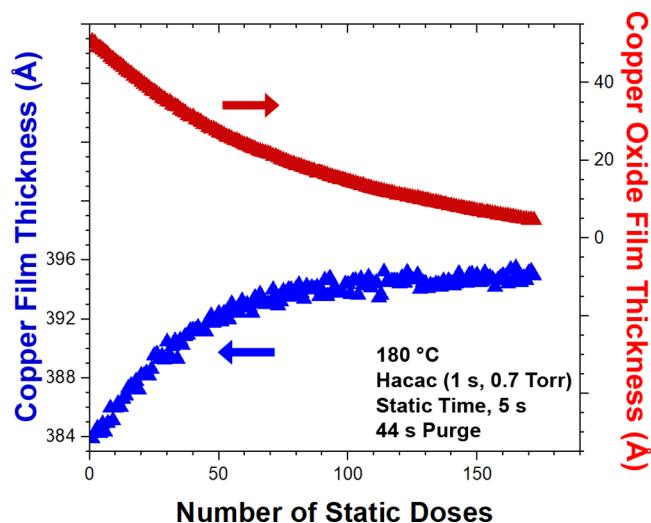


Figure 14. Film thicknesses of copper film (blue, left) and copper oxide film (right, red) versus number of static Hacac doses showing disproportionation at 180 °C.

measurements of the decrease in the copper oxide film thickness (right, red) and the increase in the metallic Cu film thickness (blue, left) during various numbers of static Hacac exposures at 180 °C. As the ~45 Å thickness of Cu₂O is removed from the underlying Cu film, there is a corresponding increase of ~12 Å of Cu metal thickness. This complementary behavior between the copper oxide and metallic copper film thicknesses is consistent with the Cu₂O disproportionation. Similar results were observed at 250 °C with the Cu₂O film rapidly undergoing disproportionation after only two Hacac exposures. Earlier studies also observed the formation of copper metal after etching Cu₂O films using Hhfac at 270 °C.³³

3.6. Thermal Etching of Other Metal Oxides with Hacac and O₃. Other first row transition metal oxides were also observed to etch when exposed to Hacac at 250 °C. Results for Sc₂O₃, NiO and Fe₃O₄ are discussed in the Supporting Information. Sc₂O₃ and NiO produced volatile acetylacetonate etch products in the same oxidation state as the initial metal oxide. Fe₃O₄ produced acetylacetonate etch products in both the +3 and +2 oxidation states. QMS results for the various etch products are given in the Supporting Information. A detailed study for CoO ALE using sequential Hacac and O₃ exposures was reported earlier.²⁷

Figure 15 summarizes this survey of all the first row transition metal oxides of a given oxidation state that were exposed to Hacac at 250 °C. Most of these first row transition metal oxides were thermally etched by Hacac exposures. ZnO, Mn₂O₃ and MnO displayed continuous, unrestricted etching by Hacac exposures. The other metal oxides displayed various degrees of limiting, restricted etching by Hacac.

Understanding why some metal oxides etch continuously and other metal oxides display limiting etching versus Hacac exposure is dependent on the Hacac reaction. Decomposition of Hacac could block the etching reaction. Combustion of Hacac could reduce the oxidation state of the metal oxide. Predicting the decomposition or combustion of Hacac will

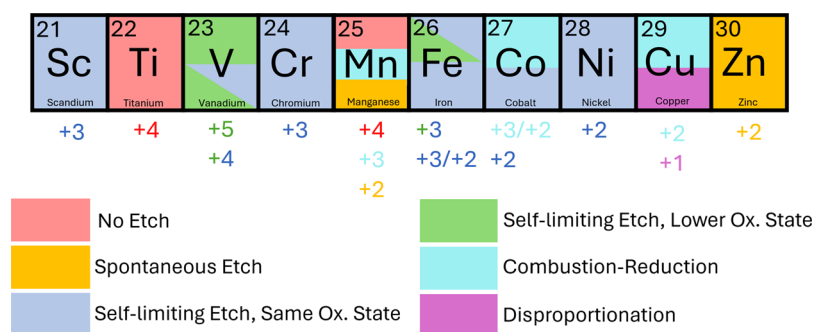


Figure 15. Summary of metal acetylacetonates formed from initial metal oxides of a given oxidation state during Hacac exposure at 250 °C.

require theoretical efforts that are beyond the scope of this paper.^{49,50}

Only TiO₂ and MnO₂ were not etched by Hacac exposure. TiO₂ and MnO₂ are both stable metal oxides in the +4 oxidation state. They would both need to be reduced to avoid forming the more sterically unfavorable M(acac)₄ complexes. Their etching may be prevented by their inability to be reduced by Hacac combustion.

4. CONCLUSIONS

Acetylacetonone (Hacac) and ozone (O₃) exposures were explored for the thermal etching of first row transition metal oxides at 250 °C. A variety of metal oxides were surveyed including Sc₂O₃, V₂O₅, VO₂, Cr₂O₃, Mn₂O₃, MnO, Fe₂O₃, Fe₃O₄, Co₃O₄, CoO, NiO, CuO, Cu₂O, and ZnO. Etching was assessed by the formation of volatile M(acac)_x etch products as observed by quadrupole mass spectrometry (QMS). Continuous, unrestricted thermal etching was monitored during multiple Hacac minidoses for ZnO, Mn₂O₃ and MnO. The other metal oxides displayed different amounts of limiting, restrictive behavior during multiple Hacac minidoses. MnO₂ and TiO₂ displayed no etching with Hacac.

The time-resolved ion intensities for the etch products during five sequential Hacac minidoses were used to determine the limiting, restrictive behavior. The M(acac)_x etch products were found in either the same oxidation state or lower oxidation state than the metal in the original metal oxide. M(acac)_x species with the same oxidation state as the original metal oxide were observed for Sc₂O₃, Cr₂O₃, MnO, Fe₂O₃, CoO, NiO, CuO, and ZnO. Evidence for reduction during etching was observed for V₂O₅, Mn₂O₃, and Co₃O₄. This reduction is attributed to oxygen loss from the metal oxide by Hacac combustion.

Several of the metal oxides revealed more complex behavior. Hacac exposures on VO₂ produced both VO(acac)₂ in the +4 oxidation state and V(acac)₃ in the +3 oxidation state. Hacac exposures on Fe₂O₃ yielded both Fe(acac)₃ in the +3 oxidation state and Fe(acac)₂ in the +2 oxidation state. Both oxidation and reduction occurred by disproportionation during Hacac exposures on Cu₂O. Hacac exposures led to the formation of metallic copper and Cu(acac)₂ in the +2 oxidation state.

The thermal etching of the first row transition metal oxides can be achieved without halogens using Hacac and O₃ exposures. For the metal oxides that display self-limiting etching versus Hacac exposures, sequential Hacac and O₃ exposures can define halogen-free ALE of all the corresponding elemental transition metals. For these elemental transition metals, the O₃ exposure is required to oxidize the metal to the corresponding metal oxide. The O₃ exposure can also refresh

the metal oxide surface after possible Hacac decomposition or combustion.

■ ASSOCIATED CONTENT

Supporting Information

The Supporting Information is available free of charge at <https://pubs.acs.org/doi/10.1021/acs.chemmater.4c00862>.

Additional QMS results during the etching of Sc₂O₃, NiO, Fe₂O₃, Fe₃O₄, and TiO₂ powders using Hacac and O₃ exposures at 250 °C (PDF)

■ AUTHOR INFORMATION

Corresponding Author

Steven M. George – Department of Chemistry, University of Colorado, Boulder, Colorado 80309, United States;

orcid.org/0000-0003-0253-9184;

Email: Steven.George@colorado.edu

Authors

Jonathan L. Partridge – Department of Chemistry, University of Colorado, Boulder, Colorado 80309, United States;

orcid.org/0000-0002-0071-9854

Aziz I. Abdulgatov – Department of Chemistry, University of Colorado, Boulder, Colorado 80309, United States

David R. Zywotko – Department of Chemistry, University of Colorado, Boulder, Colorado 80309, United States

Complete contact information is available at:

<https://pubs.acs.org/doi/10.1021/acs.chemmater.4c00862>

Notes

The authors declare no competing financial interest.

■ ACKNOWLEDGMENTS

This work was supported in part by the Joint University Microelectronics Program (JUMP) funded by the Semiconductor Research Corporation (SRC). Funding for the QMS reactor and the QMS investigations was provided by Lam Research Corporation.

■ REFERENCES

- (1) Fischer, A.; Routzahn, A.; George, S. M.; Lill, T. Thermal Atomic Layer Etching: A Review. *J. Vac. Sci. Technol., A* **2021**, *39*, No. 030801.
- (2) Kanarik, K. J.; Lill, T.; Hudson, E. A.; Sriraman, S.; Tan, S.; Marks, J.; Vahedi, V.; Gottscho, R. A. Overview of Atomic Layer Etching in the Semiconductor Industry. *J. Vac. Sci. Technol. A* **2015**, *33*, No. 020802.
- (3) George, S. M. Mechanisms of Thermal Atomic Layer Etching. *Acc. Chem. Res.* **2020**, *53*, 1151–1160.

- (4) George, S. M.; Lee, Y. Prospects for Thermal Atomic Layer Etching Using Sequential, Self-Limiting Fluorination and Ligand-Exchange Reactions. *ACS Nano* **2016**, *10*, 4889–4894.
- (5) Lee, Y.; George, S. M. Atomic Layer Etching of Al₂O₃ Using Sequential, Self-Limiting Thermal Reactions with Sn(acac)₂ and Hydrogen Fluoride. *ACS Nano* **2015**, *9*, 2061–2070.
- (6) Cano, A. M.; Marquardt, A. E.; Dumont, J. W.; George, S. M. Effect of HF Pressure on Thermal Al₂O₃ Atomic Layer Etch Rates and Al₂O₃ Fluorination. *J. Phys. Chem. C* **2019**, *123*, 10346–10355.
- (7) Clancey, J. W.; Cavanagh, A. S.; Smith, J. E. T.; Sharma, S.; George, S. M. Volatile Etch Species Produced During Thermal Al₂O₃ Atomic Layer Etching. *J. Phys. Chem. C* **2020**, *124*, 287–299.
- (8) Lii-Rosales, A.; Cavanagh, A. S.; Fischer, A.; Lill, T.; George, S. M. Spontaneous Etching of Metal Fluorides Using Ligand-Exchange Reactions: Landscape Revealed by Mass Spectrometry. *Chem. Mater.* **2021**, *33*, 7719–7730.
- (9) Lii-Rosales, A.; Johnson, V. L.; Cavanagh, A. S.; Fischer, A.; Lill, T.; Sharma, S.; George, S. M. Effectiveness of Different Ligands on Silane Precursors for Ligand Exchange to Etch Metal Fluorides. *Chem. Mater.* **2022**, *34*, 8641–8653.
- (10) Lee, Y.; Dumont, J. W.; George, S. M. Trimethylaluminum as the Metal Precursor for the Atomic Layer Etching of Al₂O₃ Using Sequential, Self-Limiting Thermal Reactions. *Chem. Mater.* **2016**, *28*, 2994–3003.
- (11) Lee, Y.; George, S. M. Thermal Atomic Layer Etching of Al₂O₃, HfO₂, and ZrO₂ Using Sequential Hydrogen Fluoride and Dimethylaluminum Chloride Exposures. *J. Phys. Chem. C* **2019**, *123*, 18455–18466.
- (12) Lee, Y.; Huffman, C.; George, S. M. Selectivity in Thermal Atomic Layer Etching Using Sequential, Self-Limiting Fluorination and Ligand-Exchange Reactions. *Chem. Mater.* **2016**, *28*, 7657–7665.
- (13) Lee, Y.; George, S. M. Thermal Atomic Layer Etching of HfO₂ Using HF For Fluorination and TiCl₄ for Ligand-Exchange. *J. Vac. Sci. Technol., A* **2018**, *36*, No. 061504.
- (14) Johnson, N. R.; George, S. M. WO₃ and W Thermal Atomic Layer Etching Using "Conversion-Fluorination" and "Oxidation-Conversion-Fluorination" Mechanisms. *ACS Appl. Mater. Interfaces* **2017**, *9*, 34435–34447.
- (15) Abdulagatov, A. I.; George, S. M. Thermal Atomic Layer Etching of Silicon Using O₂, HF, and Al(CH₃)₃ as the Reactants. *Chem. Mater.* **2018**, *30*, 8465–8475.
- (16) DuMont, J. W.; Marquardt, A. E.; Cano, A. M.; George, S. M. Thermal Atomic Layer Etching of SiO₂ by a "Conversion-Etch" Mechanism Using Sequential Reactions of Trimethylaluminum and Hydrogen Fluoride. *ACS Appl. Mater. Interfaces* **2017**, *9*, 10296–10307.
- (17) Abdulagatov, A. I.; George, S. M. Thermal Atomic Layer Etching of Silicon Nitride Using an Oxidation and "Conversion Etch" Mechanism. *J. Vac. Sci. Technol., A* **2020**, *38*, No. 022607.
- (18) Abdulagatov, A. I.; Sharma, V.; Murdzek, J. A.; Cavanagh, A. S.; George, S. M. Thermal Atomic Layer Etching of Germanium-Rich SiGe Using an Oxidation and "Conversion-Etch" Mechanism. *J. Vac. Sci. Technol., A* **2021**, *39*, No. 022602.
- (19) Green, M. L. H. A New Approach to the Formal Classification of Covalent Compounds of the Elements. *J. Organomet. Chem.* **1995**, *500*, 127–148.
- (20) Murdzek, J. A.; Lii-Rosales, A.; George, S. M. Thermal Atomic Layer Etching of Nickel Using Sequential Chlorination and Ligand-Addition Reactions. *Chem. Mater.* **2021**, *33*, 9174–9183.
- (21) Murdzek, J. A.; Lii-Rosales, A.; George, S. M. Thermal Atomic Layer Etching of Cobalt Using Sulfuryl Chloride for Chlorination and Tetramethylethylenediamine or Trimethylphosphine for Ligand Addition. *J. Vac. Sci. Technol., A* **2023**, *41*, No. 032603.
- (22) Partridge, J. L.; Murdzek, J. A.; Johnson, V. L.; Cavanagh, A. S.; Fischer, A.; Lill, T.; Sharma, S.; George, S. M. Thermal Atomic Layer Etching of CoO, ZnO, Fe₂O₃, and NiO by Chlorination and Ligand Addition Using SO₂Cl₂ and Tetramethylethylenediamine. *Chem. Mater.* **2023**, *35*, 2058–2068.
- (23) Chen, J. K. C.; Altieri, N. D.; Kim, T.; Chen, E.; Lill, T.; Shen, M. H.; Chang, J. P. Directional Etch of Magnetic and Noble Metals. *II. Organic Chemical Vapor Etch. J. Vac. Sci. Technol., A* **2017**, *35*, No. 05C305.
- (24) Mohimi, E.; Chu, X. I.; Trinh, B. B.; Babar, S.; Girolami, G. S.; Abelson, J. R. Thermal Atomic Layer Etching of Copper by Sequential Steps Involving Oxidation and Exposure to Hexafluoroacetylacetone. *ECS J. Solid State Sci. Technol.* **2018**, *7*, P491–P495.
- (25) Konh, M.; He, C.; Lin, X.; Guo, X.; Pallem, V.; Opila, R. L.; Teplyakov, A. V.; Wang, Z.; Yuan, B. Molecular Mechanisms of Atomic Layer Etching of Cobalt With Sequential Exposure to Molecular Chlorine and Diketones. *J. Vac. Sci. Technol., A* **2019**, *37*, No. 021004.
- (26) Marneli, A.; Verheijen, M. A.; Mackus, A. J. M.; Kessels, W. M. M.; Roozeboom, F. Isotropic Atomic Layer Etching of ZnO Using Acetylacetone and O₂ Plasma. *ACS Appl. Mater. Interfaces* **2018**, *10*, 38588–38595.
- (27) Partridge, J. L.; Abdulagatov, A. I.; Sharma, V.; Murdzek, J. A.; Cavanagh, A.; George, S. M. Thermal Atomic Layer Etching of CoO Using Acetylacetone and Ozone: Evidence for Changes in Oxidation State and Crystal Structure During Sequential Exposures. *Appl. Surf. Sci.* **2023**, *638*, No. 157923.
- (28) Drees, S. R.; Kodas, T. T.; Hampden-Smith, M. J. Dry Etching of ZnO Films with Hexafluoroacetylacetone. *Adv. Mater.* **1998**, *10*, 1129–1133.
- (29) George, M. A.; Hess, D. W.; Beck, S. E.; Young, K.; Bohling, D. A.; Voloshin, G.; Lane, A. P. Reaction of 1,1,1,5,5,5-Hexafluoro-2,4-Pentanedione (Hhfac) with Iron and Iron Oxide Thin Films. *J. Electrochem. Soc.* **1996**, *143*, 3257–3266.
- (30) Kytokivi, A.; Rautiainen, A.; Root, A. Reaction of Acetylacetone Vapour with Gamma-Alumina. *J. Chem. Soc., Faraday Trans.* **1997**, *93*, 4079–4084.
- (31) Farkas, J.; Chi, K. M.; Hampden-Smith, M. J.; Kodas, T. T.; Dubois, L. H. Etching of Copper and Copper-Oxide at High-Rates via Generation of Volatile Copper Species. *Mater. Sci. Eng., B* **1993**, *17*, 93–96.
- (32) George, M. A.; Hess, D. W.; Beck, S. E.; Ivankovits, J. C.; Bohling, D. A.; Lane, A. P. Reaction of 1,1,1,5,5,5-Hexafluoro-2,4-Pentanedione (Hhfac) with CuO, Cu₂O, and Cu Films. *J. Electrochem. Soc.* **1995**, *142*, 961–965.
- (33) Rousseau, F.; Jain, A.; Kodas, T. T.; Hampden-Smith, M.; Farr, J. D.; Muenchausen, R. Low-Temperature Dry Etching of Metal-Oxides and ZnS via Formation of Volatile Metal Beta-Diketonate Complexes. *J. Mater. Chem.* **1992**, *2*, 893–894.
- (34) Kang, S. W.; Kim, H. U.; Rhee, S. W. Dry Etching of Copper Film with Hexafluoroacetylacetone via Oxidation Process. *J. Vac. Sci. Technol. B* **1999**, *17*, 154–157.
- (35) Lee, W.; Yang, H. J.; Reucroft, P. J.; Soh, H. S.; Kim, J. H.; Woo, S. L.; Lee, J. Dry Patterning of Copper Films Using an O₂ Plasma and Hexafluoroacetylacetone. *Thin Solid Films* **2001**, *392*, 122–127.
- (36) Jain, A.; Kodas, T. T.; Hampden-Smith, M. J. Thermal Dry-Etching of Copper Using Hydrogen Peroxide and Hexafluoroacetylacetone. *Thin Solid Films* **1995**, *269*, 51–56.
- (37) Steger, R.; Masel, R. Chemical Vapor Etching of Copper Using Oxygen and 1,1,1,5,5,5-Hexafluoro-2,4-Pentanedione. *Thin Solid Films* **1999**, *342*, 221–229.
- (38) Elam, J. W.; Groner, M. D.; George, S. M. Viscous Flow Reactor with Quartz Crystal Microbalance for Thin Film Growth by Atomic Layer Deposition. *Rev. Sci. Instrum.* **2002**, *73*, 2981–2987.
- (39) Zywojtko, D. R.; George, S. M. Thermal Atomic Layer Etching of ZnO by a "Conversion-Etch" Mechanism Using Sequential Exposures of Hydrogen Fluoride and Trimethylaluminum. *Chem. Mater.* **2017**, *29*, 1183–1191.
- (40) Fernelius, W. C.; Blanch, J. E. Chromium(III) Acetylacetonate [Tris(2,4-Pentanedione)Chromium(III)]. *Inorg. Synth.* **1957**, *5*, 130–131.

- (41) Melia, T. P.; Merrifield, R. Vapour Pressures of the Tris(Acetylacetonato) Complexes of Scandium(III), Vanadium(III) and Chromium(III). *J. Inorg. Nucl. Chem.* **1970**, *32*, 1489–1493.
- (42) Wallace, W. E. *Mass Spectrum of Chromic Acetylacetonate*; NIST Chemistry WebBook, NIST SRD Number 69, 2014.
- (43) Tynell, T.; Karppinen, M. Atomic Layer Deposition of ZnO: A Review. *Semicond. Sci. Technol.* **2014**, *29*, No. 043001.
- (44) Wang, Y.; Su, Q.; Chen, C. H.; Yu, M. L.; Jhan, G.; Wang, G. Q.; Xin, K.; Lan, W.; Liu, X. Q. Low Temperature Growth of Vanadium Pentoxide Nanomaterials by Chemical Vapour Deposition Using VO(acac)₂ as Precursor. *J. Phys. D* **2010**, *43*, No. 18S102.
- (45) Ereztech Website. [Ereztech.com](http://ereztech.com) (Accessed July 11, 2024), Manganese Acetylacetonate.
- (46) Wallace, W. E. *Mass Spectrum of Manganic Acetylacetonate*; NIST Chemistry WebBook, NIST SRD Number 69, 2014.
- (47) Shibata, S.; Onuma, S.; Inoue, H. Crystal and Molecular-Structure of Trimeric Bis(Acetylacetonato)Manganese(II). *Inorg. Chem.* **1985**, *24*, 1723–1725.
- (48) Schneider, J. R.; de Paula, C.; Richey, N. E.; Baker, J. G.; Oyakhire, S. T.; Bent, S. F. Understanding and Utilizing Reactive Oxygen Reservoirs in Atomic Layer Deposition of Metal Oxides with Ozone. *Chem. Mater.* **2022**, *34*, 5584–5597.
- (49) Basher, A. H.; Krstic, M.; Fink, K.; Ito, T.; Karahashi, K.; Wenzel, W.; Hamaguchi, S. Formation and Desorption of Nickel Hexafluoroacetylacetonate Ni(Hfac)₂ on a Nickel Oxide Surface in Atomic Layer Etching Processes. *J. Vac. Sci. Technol., A* **2020**, *38*, No. 052602.
- (50) Kung, H.; Teplyakov, A. Selectivity and Mechanism of Thermal Decomposition of β -Diketones on ZnO Powder. *J. Catal.* **2015**, *330*, 145–153.